JMEPEG (2012) 21:2695–2700
DOI: 10.1007/s11665-012-0308-y

1059-9495/$19.00

Comparative In Vitro Study of Ti-12V-9Sn Shape Memory Alloy with C.P. Ti and Ti-12V Alloy for Potential Biomedical Application

K.J. Qiu, B.L. Wang, F.Y. Zhou, W.J. Lin, L. Li, J.P. Lin, and Y.F. Zheng

(Submitted March 19, 2012; in revised form June 28, 2012)

The microstructure, mechanical properties, and electrochemical behavior of Ti-12V-9Sn shape memory alloy were investigated, with commercial pure titanium (C.P. Ti) and Ti-12V alloy as controls. The metastable β phase was partially retained and α″ martensite phase was obtained in Ti-12V-9Sn alloy, whereas only martensitic phases (α′ and α″) existed in Ti-12V alloy at room temperature. Ti-12V-9Sn alloy exhibited a good combination of strength and elongation, which showed a "double yield" feature, along with a complete shape recovery strain of 4%. The electrochemical measurements indicated that all of the experimental samples exhibited excellent corrosion resistance in the artificial saliva with and without 0.2% NaF, among which Ti-12V-9Sn alloy possessed the lowest corrosion current density in both kinds of simulated body fluids.

Keywords electrochemical measurements, mechanical properties, microstructure, shape memory materials, Ti-V-Sn alloy

1. Introduction

During the past few decades, titanium and its alloys have been extensively used in biomedical fields because of their low density, excellent corrosion resistance, and superior biocompatibility (Ref 1). However, the low strength and the poor wear resistance of commercial pure (C.P.) Ti restrict its use in a lot of applications, especially where high mechanical property is required. Recently, many Ti-based shape memory alloys such as Ti-Nb-based (Ref 2, 3) and Ti-Mo-based (Ref 4) alloys have been developed for biomedical applications. It is also found that Ti-10V-2Fe-3Al (Ref 5, 6) exhibited shape memory effect. Matsumoto et al. (Ref 7-9) studied the Ti-V-Sn alloys (mainly with 8 wt.% V), and the results indicated that addition of Sn to Ti-V alloy was favorable for increasing ductility while keeping its low Young's modulus and high strength. It seems quite suitable for biomedical application, yet in vitro biocorrosion evaluation has not been done in the simulated body fluid. In the present study, focus was placed on the microstructure, mechanical properties, and electrochemical behavior of the Ti-12V-9Sn shape memory alloy, which was studied for the first time from the viewpoint of biomaterials, with the C.P. Ti and Ti-12V alloy as controls.

This article is an invited paper selected from presentations at the International Conference on Shape Memory and Superelastic Technologies 2011, held November 6-9, 2011, in Hong Kong, China, and has been expanded from the original presentation.

K.J. Qiu, B.L. Wang, F.Y. Zhou, W.J. Lin, and **L. Li**, Center for Biomedical Materials and Engineering, Harbin Engineering University, Harbin, China; **J.P. Lin**, State Key Laboratory for Advanced Metals and Materials, University of Science and Technology Beijing, Beijing 100083, China; and **Y.F. Zheng**, Center for Biomedical Materials and Engineering, Harbin Engineering University, Harbin, China; and Department of Materials Science and Engineering, College of Engineering, Peking University, Beijing, China. Contact e-mail: yfzheng@pku.edu.cn.

2. Materials and Methods

The experimental Ti-12V and Ti-12V-9Sn (wt.%) alloys were prepared by arc melting process in an argon atmosphere. The resulting arc-melted buttons were hot-rolled into plates with 7.5 mm in thickness and then cold-rolled into plates with the final thickness of 1.5 mm. The commercial pure titanium (Grade 2 C.P. Ti, 99% in purity, hot-rolled, provided by Xi'an Saite Metal Materials Development CO., LTD, China) was used in this study as control. The experimental cold-rolled Ti alloys' plates and C.P. Ti were solution treated at 850 °C for 30 min and quenched in ice water.

The microstructures were identified by optical microscopy (BX51M, Olympus, Japan). XRD patterns were obtained by X'Pert Pro diffractometer at 40 kV and 40 mA. DSC measurements were conducted on Perkin Elmer Diamond with a scan rate of 30 °C/min. Tensile tests were carried out on Instron 3365 with an initial strain rate of 8.3×10^{-4}/s at room temperature. The morphology of fracture surface was examined by scanning electron microscope (SEM, Cambridge S240). The shape memory effect was evaluated by loading and unloading cyclic tensile tests (Ref 6). The microhardness of specimens was measured at 500 g for 15 s, using a digital hardness tester (HVS-1000), repeating five times in different positions for each sample to get an average value.

The electrochemical measurements were conducted using CHI660C electrochemical working station at 37 °C. The

Fuayama Mayer artificial saliva (NaCl 0.4 g/L; KCl 0.4 g/L; $CaCl_2$ 0.6004 g/L; $NaH_2PO_4 \cdot 2H_2O$ 0.78 g/L; KSCN 0.300 g/L; $Na_2S \cdot 9H_2O$ 0.005 g/L; and urea 1.000 g/L) with and without 0.2% NaF were used in the testing (Ref 10). A platinum counter electrode and an Ag/AgCl reference electrode were used for electrochemical tests, and the experimental sample was used as working electrode. Electrochemical impedance spectroscopy (EIS) measurement was begun after an immersion time of 7.2×10^3 s. The impedance data were analyzed and fitted to appropriate equivalent electrical circuit using the ZSimpWin software. The potentiodynamic polarization test was measured from −0.8 to 1.5 V with a scan rate of 1 mV/s, after the above mentioned EIS test. Corrosion parameters including corrosion potential (E_{corr}) and corrosion current density (I_{corr}) can be estimated by Tafel analysis based on the polarization plots.

3. Results and Discussion

Figure 1(a) and (b) shows the optical micrographs of Ti-12V and Ti-12V-9Sn alloys, respectively. It can be seen that plenty of lamellar microstructure appeared in both Ti-12V and Ti-12V-9Sn alloys at room temperature, but the average grain size of Ti-12V-9Sn alloy is smaller than that of Ti-12V alloy. Figure 2 shows the corresponding XRD patterns of Ti-12V and Ti-12V-9Sn alloys. α′ (hcp) and α″ (orthorhombic) martensite phases can be identified in Ti-12V alloy, and the lamellar structure observed in Fig. 1(a) is considered to be α′ and α″ martensite, which is consistent with previous report (Ref 7). However, the diffraction peaks of Ti-12V-9Sn alloy can be identified as β (bcc) phase and α″ martensite phase. The intensity of β phase peaks is much higher than that of α″ martensite phase peaks, which implied that the β phase is the dominant phase in Ti-12V-9Sn alloy at room temperature.

Three duplicate samples of Ti-12V-9Sn alloy were tested in the DSC measurements, and one of them was repeated twice with different scan rates (30 and 10 °C/min, respectively). Here, the DSC curve of Ti-12V-9Sn alloy with a scan rate of 30 °C/min is shown in Fig. 3. An obvious peak (149.36 °C) appeared on the heating curve, which could be attributed to the transformation of α″ martensite phase to β phase, while no clear peak was observed on the subsequent cooling curve (from 250 to 0 °C, even to −100 °C, and irrespective of heating at first or cooling at first). The subsequent DSC cyclic measurement shows that the heating peak appeared only at the first

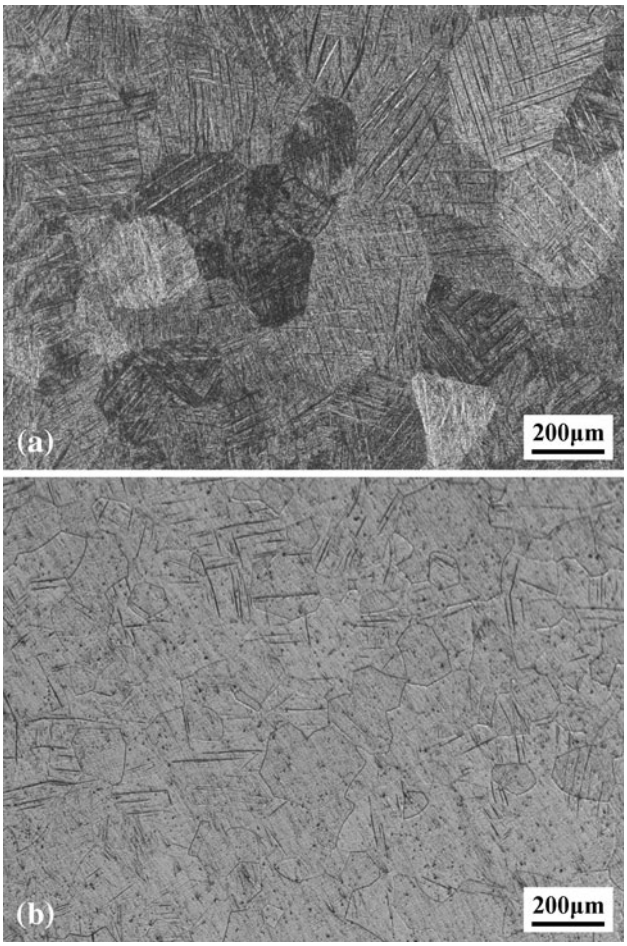

Fig. 1 Optical micrographs of (a) Ti-12V and (b) Ti-12V-9Sn alloys

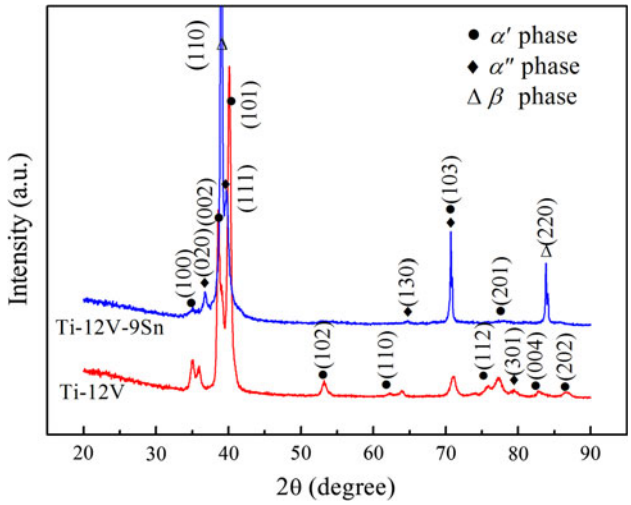

Fig. 2 XRD patterns of Ti-12V and Ti-12V-9Sn alloys

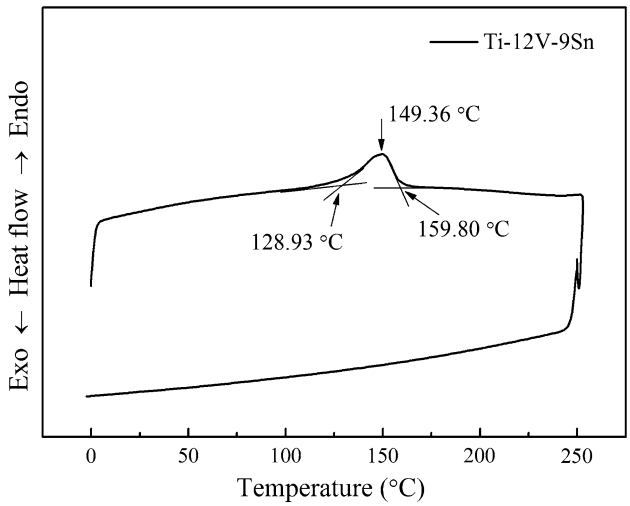

Fig. 3 DSC curves of Ti-12V-9Sn alloy with a scan rate of 30 °C/min

cycle. However, the bi-phase structure of Ti-12V-9Sn alloy shown in Fig. 2 indicates that the martensite transformation temperature (M_s) of this alloy should be higher than the ambient temperature. The fact that no peak has appeared on the cooling curve (Fig. 3) implied that the martensite transformation (β martensite phase to α″ phase) could not occur so quickly during the testing time. The same heating peak would be detected again when the same tested sample was placed for a few days in the air, which is deemed to effect the completion of martensitic transformation at that time. In other words, the martensitic transformation is assumed to be controlled by kinetics. Therefore, no difference was observed when the same sample was tested at different times.

The tensile stress-strain curves of C.P. Ti, Ti-12V, and Ti-12V-9Sn alloys are shown in Fig. 4(a). Ti-12V alloy possessed the highest strength and the smallest elongation, whereas C.P. Ti had the lowest strength and the greatest elongation. Ti-12V-9Sn alloy exhibited the excellent combination of strength (UTS = 634 MPa) and elongation (32.5%). Furthermore, the double yielding phenomenon was observed in the tensile test of Ti-12V-9Sn alloy. The first yielding might be related to the stress-induced martensitic transformation, and the second yielding might be the result of plastic deformation of β or α″ presumably, which was similar to that of the Ti-10V-2Fe-3Al alloy (Ref 6).

Ti-12V-9Sn alloy exhibited the superelasticity during loading and unloading cyclic tensile tests, as shown in Fig. 4(b). The cyclic tensile test was carried out at room temperature by constant strain increment of 2% per loading-unloading cycle under the initial strain rate of 8.3×10^{-4}/s. The recovery strain with the reverse transformation of stress-induced martensite is defined as ε_{SIMT}, and the total recovery strain with superelasticity is defined as ε_{SE}, as indicated in Fig. 4(b). The recovery strain increases with the increasing applied strain in Ti-12V-9Sn alloy. The maximum ε_{SE} was about 3.5% which contains about 1.2% ε_{SIMT}, where the applied strain was 10%. Figure 4(c) shows the series of stress-strain curves of Ti-12V-9Sn samples by loading and unloading tensile tests. After unloading, the specimens are heated to above 200 °C, and the dashed lines with arrows denote the shape memory recovery strain by heating. Obvious shape memory effect can be observed for all the curves. 100% shape recovery is exhibited at 4% applied strain, and the permanent strain increases with the increasing applied strain. The maximum recoverable strain is about 6%, when the applied strains are 8 and 10%, respectively.

The mechanical properties (including 0.2% proof stress, ultimate tensile strength, and elongation to fracture) of the experimental samples are marked in Fig. 5(a). The microhardness values of C.P. Ti, Ti-12V, and Ti-12V-9Sn alloys are shown in Fig. 5(b). It could be found that the microhardness values of Ti-12V alloy (506 HV) and Ti-12V-9Sn alloy (311 HV) were much higher than that of C.P. Ti (183 HV).

The SEM images of the fracture surface morphologies of C.P. Ti, Ti-12V, and Ti-12V-9Sn alloys after tensile tests are shown in Fig. 6. The C.P. Ti and Ti-12V-9Sn alloys exhibited typical ductile fracture with fine equiaxed dimples, whereas Ti-12V alloy indicated a mixture pattern of dimple- and facets-like cleavage fracture plane, which illustrated the significant differences of mechanical properties for these three materials on microscopic fracture mechanism.

Figure 7 shows the representative EIS spectra plots of C.P. Ti, Ti-12V, and Ti-12V-9Sn alloys after 2-h immersion in the two different electrolytes. The $R_S(Q_PR_P)$ equivalent circuit

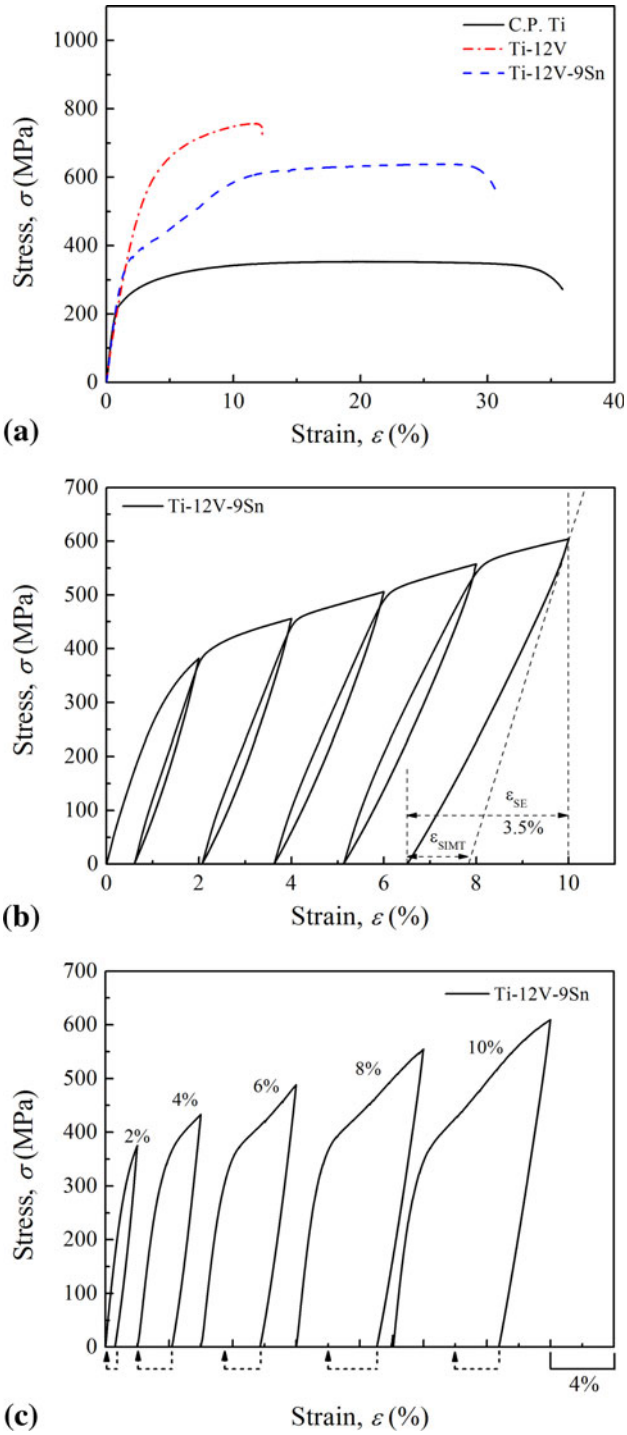

Fig. 4 (a) Stress-strain curves of C.P. Ti, Ti-12V, and Ti-12V-9Sn alloys; (b, c) stress-strain curves obtained from cyclic tensile test in Ti-12V-9Sn alloy

model with only one time constant was proposed to fit the EIS data, where R_S is the electrolyte resistance, Q_P is the constant phase element (which represents a true capacitance, rather than an ''ideal'' capacitance C), and R_P is the resistance of passive film. The parameters (R_S, Q_P, n, and R_P) obtained by the fitting procedure are listed in Table 1. The good consistence between the experimental data and fitted data was obtained with the χ^2 of about 10^{-4}.

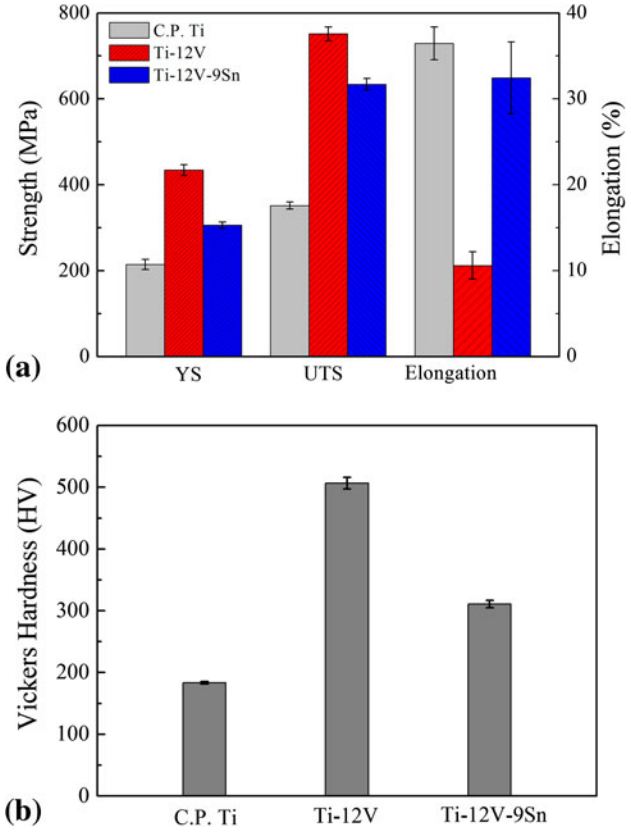

Fig. 5 (a) mechanical properties and (b) microhardness of C.P. Ti, Ti-12V, and Ti-12V-9Sn alloys

From Fig. 7(a) and (c), it can be seen obviously that Ti-12V alloy possessed a smaller diameter of the semicircle, and Ti-12V-9Sn alloy performed a larger one compared with C.P. Ti, especially in artificial saliva with 0.2% NaF, whereas Ti-12V alloy had a worse corrosion resistance and Ti-12V-9Sn alloy had a better one in comparison with C.P. Ti (Ref 11). From the Bode-magnitude plots shown in Fig. 7(b) and (d), it can be seen that there were two distinct regions for all the samples immersed in both the electrolytes. In the high-frequency range (10^2-10^4 Hz), a flat portion of curves (slope ≈ 0) was observed, which is due to the response of electrolyte resistance. In the low- and middle-frequency ranges, the curves displayed a linear slope of about -1, which is the characteristic response of a capacitive behavior of passive film (Ref 11, 12).

There are three characteristic regions for all the samples in the Bode-phase angle plots in Fig. 7(b) and (d). In the high-frequency range, the phase angle dropped to 0° with the response of electrolyte resistance; in the middle frequency, the phase angle was found to be of approximately −80°, indicating a typical passive film being presented on the surface and a near capacitive response for passive film; in the low-frequency range, the phase angle decreased to lower value because of the contribution of the passive film resistance (Ref 11). The evidence presented in Fig. 7 confirmed that the addition of V decreased the corrosion resistance, and the addition of Sn increased the corrosion resistance of the passive film of titanium in the artificial saliva with and without 0.2% NaF.

Figure 8 shows the potentiodynamic polarization curves for C.P. Ti, Ti-12V, and Ti-12V-9Sn alloys after 2-h immersion in

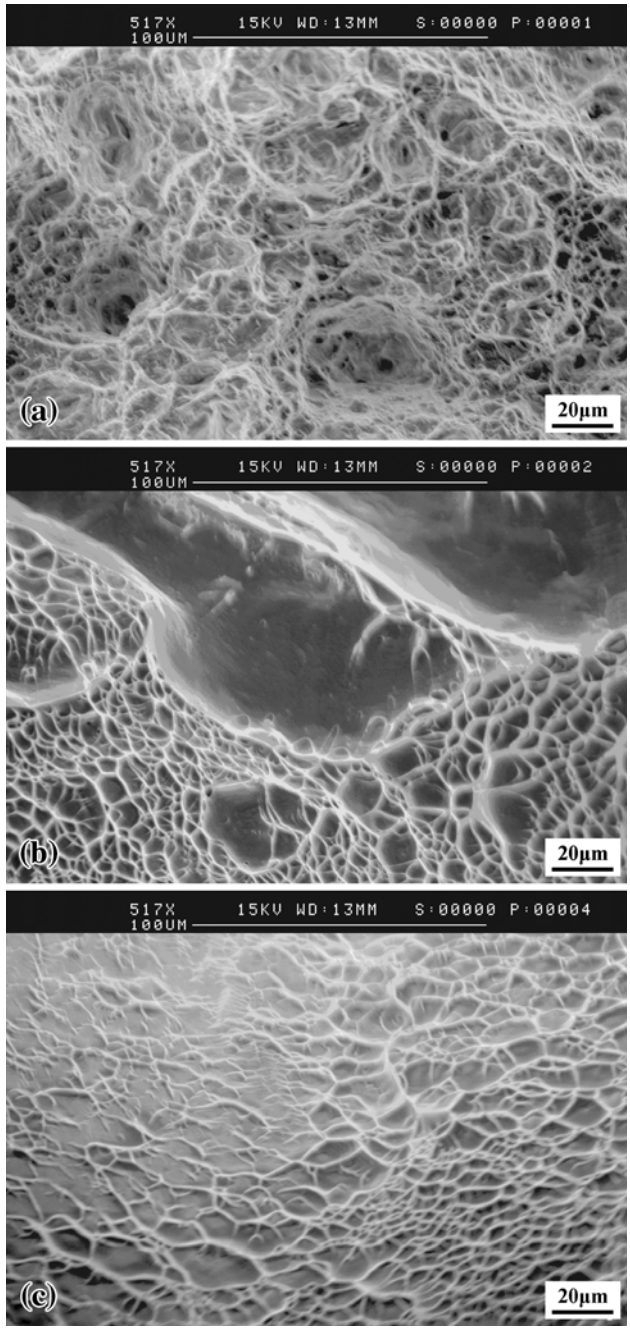

Fig. 6 SEM images of fracture surface of (a) C.P. Ti, (b) Ti-12V, and (c) Ti-12V-9Sn alloys

the artificial saliva with two different NaF concentrations (0 and 0.2%). The corrosion potentials (E_{corr}) and corrosion current densities (I_{corr}) were estimated by Tafel plots, which are listed in Table 2. In the artificial saliva, the I_{corr} values of Ti-12V alloy (0.093 μA/cm^2) and Ti-12V-9Sn alloy (0.047 μA/cm^2) are lower than that of C.P. Ti (0.11 μA/cm^2). In the artificial saliva with 0.2% NaF, the variation of I_{corr} had a similar trend, i.e., I_{corr} values of Ti-12V alloy (0.079 μA/cm^2) and Ti-12V-9Sn alloy (0.057 μA/cm^2) are lower than that of C.P. Ti (0.14 μA/cm^2). It is worth noting that there are broad and distinctive passivation regions for all the experimental samples

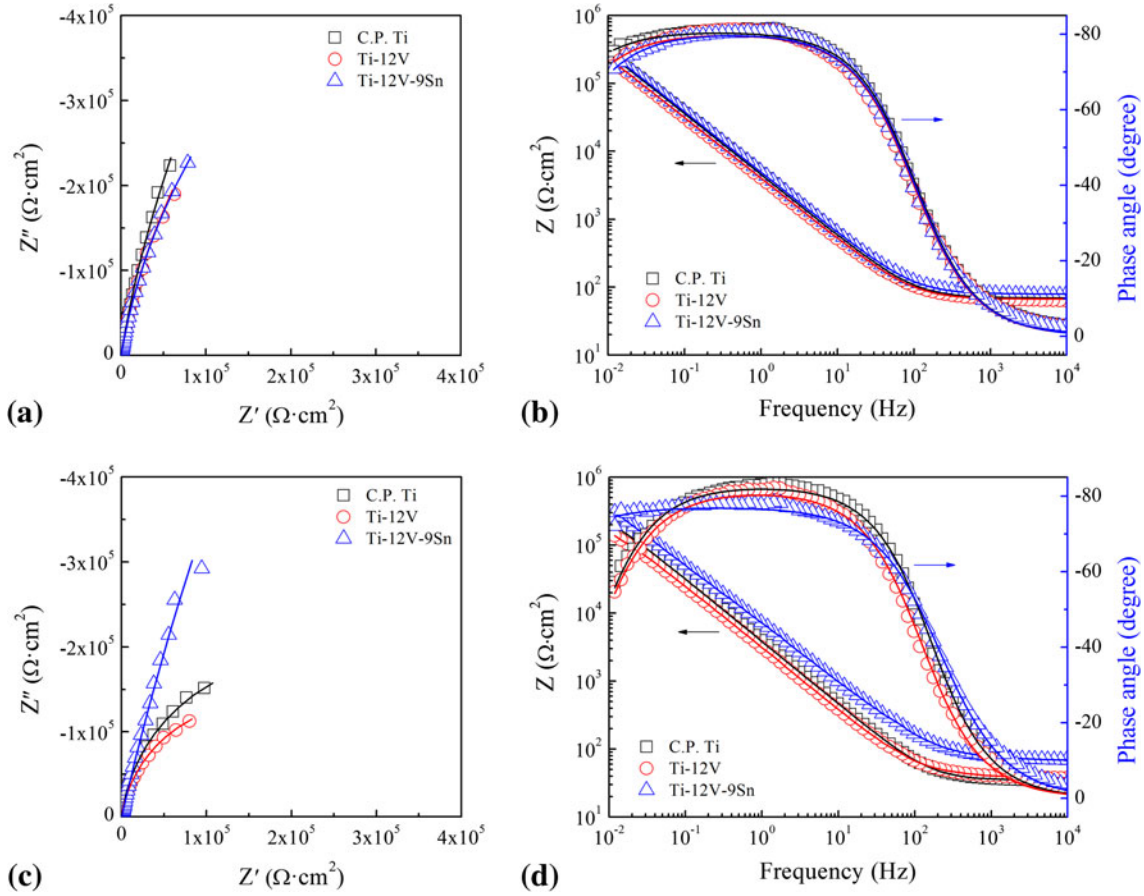

Fig. 7 Representative EIS spectra plots of C.P. Ti, Ti-12V, and Ti-12V-9Sn alloys. (a) Nyquist plots and (b) Bode plots in artificial saliva; (c) Nyquist plots and (d) Bode plots in artificial saliva with 0.2% NaF (all fitted data were shown in lines)

Table 1 Electrochemical impedance parameters of C.P. Ti, Ti-12V, and Ti-12V-9Sn alloys in artificial saliva without (AS) and with 0.2% NaF (AS + 0.2%F), respectively

Materials	Electrolytes	R_S, Ω cm^2	Q_P, μA/cm^2	n	R_P, 10^5 Ω cm^2	χ^2, 10^{-4}
C.P. Ti	AS	69.26	42.28	0.90	2.72	8.84
	AS + 0.2%F	35.11	47.87	0.92	4.15	8.08
Ti-12V	AS	66.59	38.90	0.89	2.65	9.50
	AS + 0.2%F	39.34	61.11	0.91	3.05	10.05
Ti-12V-9Sn	AS	80.72	51.01	0.89	3.22	4.81
	AS + 0.2%F	36.03	50.82	0.88	4.57	5.27

(up to 1.3 V), which indicated that the passive films formed on the surface of samples were stable and protective. However, the passivation current densities (I_{pass}) were in the ranges of 5.4-6.5 μA/cm^2 for Ti-12V alloy and 3.1-5.4 μA/cm^2 for Ti-12V-9Sn alloy compared with the range of 4.6-6.7 μA/cm^2 for C.P. Ti in artificial saliva, and in the artificial saliva with 0.2% NaF, the I_{pass} values were in the ranges of 9.4-11.2 μA/cm^2 for Ti-12V alloy and 6.4-10.8 μA/cm^2 for Ti-12V-9Sn alloy, whereas the corresponding range was 8.2-10.8 μA/cm^2 for C.P. Ti. Comparing Fig. 8(a) with (b), it can be seen that there were no significant differences in corrosion resistances with and without 0.2% NaF artificial saliva, and all the experimental samples exhibited the excellent corrosion resistance in both solutions. The results were in good agreement with the EIS results, which indicated that adding V into Ti lowered the corrosion resistance, whereas adding Sn into Ti would improved the corrosion resistance in artificial saliva (with and without 0.2% NaF).

4. Conclusions

Ti-12V alloy consists of α′ and α″ phases, whereas Ti-12V-9Sn alloy comprises the β and α″ phases at room temperature. Ti-12V alloy showed the highest strength, while C.P. Ti possessed the highest elongation. Ti-12V-9Sn alloy exhibited the best combination of strength and elongation, which also showed shape memory effect, with a complete shape recovery strain of 4%. All the experimental samples showed excellent corrosion resistance, among which Ti-12V-9Sn alloy possessed

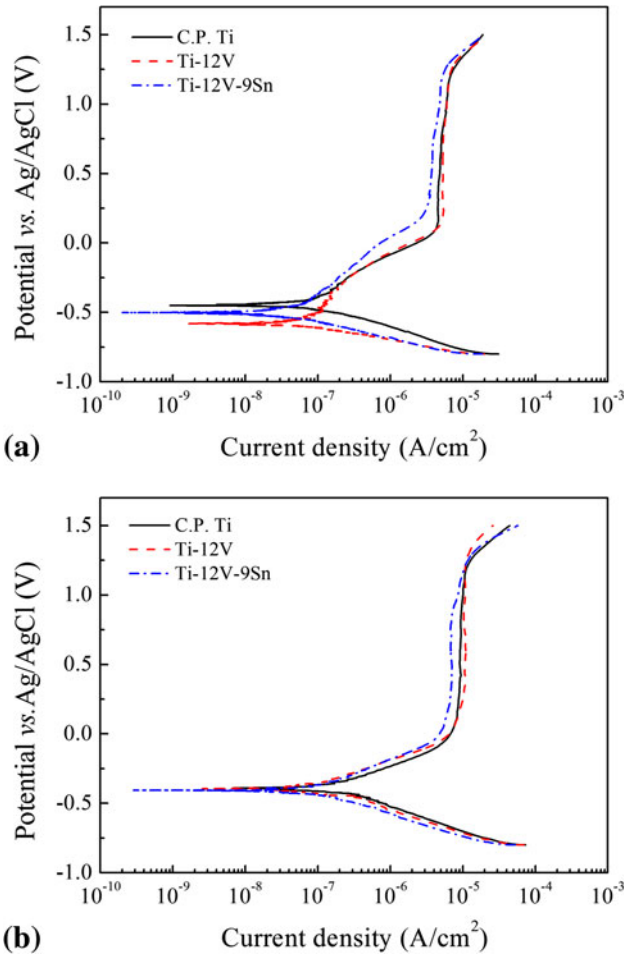

Fig. 8 The potential dynamic polarization curves of C.P. Ti, Ti-12V and Ti-12V-9Sn alloys in (a) artificial saliva and (b) artificial saliva with 0.2% NaF, respectively

Table 2 Corrosion parameters of C.P. Ti, Ti-12V, and Ti-12V-9Sn alloys in artificial saliva without (AS) and with 0.2% NaF (AS + 0.2%F), respectively

Materials	Electrolytes	I_{corr} μA/cm^2	E_{corr} V
C.P. Ti	AS	0.114	−0.451
	AS + 0.2%F	0.137	−0.389
Ti-12V	AS	0.093	−0.583
	AS + 0.2%F	0.079	−0.394
Ti-12V-9Sn	AS	0.047	−0.502
	AS + 0.2%F	0.057	−0.409

the lowest values of I_{corr} and I_{pass}, which showed that it has the best corrosion resistance. All the above results indicated that Ti-12V-9Sn might be a potential candidate to be used as a biomedical shape memory material.

Acknowledgments

This work was supported by State Key Lab of Advanced Metals and Materials (Grant No. 2011-ZD01), National Basic Research Program of China (973 Program) (Grant No. 2012CB619102), National High Technology Research and Development Program of China (863 Program) under Grant numbers 2011AA030101 and 2011AA030103, Fundamental Research Funds for the Central University (HEUCFZ1017 and HEUCFR1020), Natural Science Foundation of Heilongjiang Province (ZD201012).

References

1. M. Geetha, A.K. Singh, R. Asokamani, and A.K. Gogia, Ti Based Biomaterials, the Ultimate Choice for Orthopaedic Implants—A Review, *Prog. Mater. Sci.*, 2009, **54**(3), p 397–425
2. Y.L. Hao, S.J. Li, S.Y. Sun, and R. Yang, Effect of Zr and Sn on Young's Modulus and Superelasticity of Ti-Nb-Based Alloys, *Mater. Sci. Eng. A*, 2006, **441**(1–2), p 112–118
3. B.L. Wang, Y.F. Zheng, and L.C. Zhao, Effects of Sn Content on the Microstructure, Phase Constitution and Shape Memory Effect of Ti-Nb-Sn Alloys, *Mater. Sci. Eng. A*, 2008, **486**(1–2), p 146–151
4. T. Maeshima, S. Ushimaru, K. Yamauchi, and M. Nishida, Effect of Heat Treatment on Shape Memory Effect and Superelasticity in Ti-Mo-Sn Alloys, *Mater. Sci. Eng. A*, 2006, **438–440**, p 844–847
5. A. Bhattacharjee, S. Bhargava, V.K. Varma, S.V. Kamat, and A.K. Gogia, Effect of β Grain Size on Stress Induced Martensitic Transformation in β Solution Treated Ti-10V-2Fe-3Al Alloy, *Scripta Mater.*, 2005, **53**, p 195–200
6. T. Furuhara, S. Annakab, Y. Tomiob, and T. Makic, Superelasticity in Ti-10V-2Fe-3Al Alloys with Nitrogen Addition, *Mater. Sci. Eng. A*, 2006, **438–440**, p 825–829
7. H. Matsumoto, S. Watanabe, and N. Masahashi, Composition Dependence of Young's Modulus in Ti-V, Ti-Nb, and Ti-V-Sn Alloys, *Metall. Mater. Trans. A*, 2006, **37**(11), p 3239–3249
8. H. Matsumoto, S. Watanabe, and S. Hanada, α′ Martensite Ti-V-Sn Alloys with Low Young's Modulus and High Strength, *Mater. Sci. Eng. A*, 2007, **448**, p 39–48
9. H. Matsumoto, A. Chiba, and S. Hanada, Anisotropy of Young's and Tensile Properties in Cold Rolled α′ Martensite Ti-V-Sn Alloys, *Mater. Sci. Eng. A*, 2008, **486**, p 503–510
10. H.H. Huang, Effects of Fluoride and Albumin Concentration on the Corrosion Behavior of Ti-6Al-4V Alloy, *Biomaterials*, 2003, **24**(2), p 275–282
11. B.L. Wang, Y.F. Zheng, and L.C. Zhao, Electrochemical Corrosion Behavior of Biomedical Ti-22Nb and Ti-22Nb-6Zr Alloys in Saline Medium, *Mater. Corros.*, 2009, **60**(10), p 788–794
12. A.W. Hodgson, Y. Mueller, D. Forster, and S. Virtanen, Electrochemical Characterisation of Passive Films on Ti Alloys Under Simulated Biological Conditions, *Electrochim. Acta*, 2002, **47**(12), p 1913–1923